Eur. Phys. J. E (2018) **41**: 41
DOI 10.1140/epje/i2018-11645-4

THE EUROPEAN PHYSICAL JOURNAL E

Regular Article

Taylor-Green vortex simulation using CABARET scheme in a weakly compressible formulation[⋆]

Yury M. Kulikov and Eduard E. Son[a]

Joint Institute for High Temperatures of RAS, Izhorskaya st. 13 Bd.2, 125412 Moscow, Russia

Received 14 August 2017 and Received in final form 19 January 2018

Abstract. In present paper we recall the canonical Taylor-Green vortex problem solved by in-house implementation of the novel CABARET numerical scheme in weakly compressible formulation. The simulations were carried out on the sequence of refined grids with 64^3, 128^3, 256^3 cells at various Reynolds numbers corresponding to both laminar ($\mathrm{Re} = 100, 280$) and turbulent ($\mathrm{Re} = 1600, 4000$) vortex decay scenarios. The features of the numerical method are discussed in terms of the kinetic energy dissipation rate and integral enstrophy curves, temporal evolution of the spanwise vorticity, energy spectra and spatial correlation functions.

1 Introduction

Taylor-Green vortex (TGV) decay being the canonical problem of the computational hydrodynamics is proved to be a useful benchmark when testing sophisticated numerical algorithms aimed for modeling of the vorticity evolution, the turbulent transition and the subsequent decay of turbulence. Generally, the evolution of TGV is accompanied by the vortex field complication when multiscale vortex structures are formed and nonlinearly interact. In the original formulation [1], the flow was analyzed using asymptotic methods, however, the series expansion based on time or Reynolds number [2] does not allow describing the flows at the advanced evolution times t or high Re. At present, the Taylor-Green problem is the object of applying a wide variety of numerical methods and models of turbulence that are distinguished by their genericity, order of accuracy, dispersion and dissipative characteristics. For the flow under consideration the spectral methods are the most competitive among others, as they utilize specialized basis functions with account for flow symmetries that significantly improve the accuracy of results and the calculation efficiency. It was Brachet *et al.* [3], which performed the first numerical simulation of the inertial interval of free turbulence using the trigonometric functions expansion and the Galerkin method.

A rapid convergence of spectral techniques provides the way to more accurate modelling of small scales. In comparison with the finite-difference methods they require at least 2 times less spectral resolution [4] in one direction or 8 times less degrees of freedom in three-dimensional calculations, if the error reaches 5–10%. However, the most computationally "expensive" procedure in this case is the correct estimate of Navier-Stokes equations right-hand side written as the sum of the pairwise products of the coefficients of the spectral expansion. Direct computation of this convolution appears to be impossible due to the strong nonlocality of the data access, which requires additional techniques to implement them successfully for massive parallel calculations [5].

Finite-difference RANS and LES methods can serve as a competitive alternative for turbulence modeling: the former successfully work on an ensemble of similar flows [6], for which well-calibrated models are developed, such as attached boundary layers and flows without strong inhomogeneities. LES algorithms [7] employing the idea of velocity splitting into a smooth averaged component (which is the subject of calculation) and a strongly oscillating component [5], directly model large-scale structures containing the main part of turbulent kinetic energy. To simulate the effects of subgrid scales, additional algorithms are used, minimizing the drawbacks of a subgrid model itself. Relatively slow grid convergence of LES methods achieved on very large and time-consuming grids [6] at medium and high Reynolds numbers is considered as the main drawback.

TGV flow modeling performed in the present paper has been motivated by several remarkable properties of the CABARET numerical scheme observed in one- and two-dimensional formulations. In particular, CABARET scheme

- has a compact computational stencil housed into one space-time cell;
- is reversible on a substantial time interval;

[⋆] Contribution to the Topical Issue "Non-equilibrium processes in multicomponent and multiphase media" edited by Tatyana Lyubimova, Valentina Shevtsova, Fabrizio Croccolo.

[a] e-mail: `kulikov-yurii@yandex.ru`

- possesses formally the second-order accuracy both at nonuniform spatial grid and time step unless nonlinear flux correction procedure is used;
- has a seamless flux correction algorithm based on direct use of Riemann's invariants;
- is universal and does not have any adjustable parameters;
- can be used to calculate both blast and ultra-weak shock waves;
- complies with aeroacoustics, wherein the sound oscillations are several orders of magnitude lower than hydrodynamic ones, while their scale [8], on the contrary, is several orders greater. In this case high-accuracy methods (such as DRP [9]) are the proved tool as they use more sparse grids and are more accurate than second-order schemes. However, high-order approximation techniques can yield incorrect solutions on variable size cells meshes;
- is capable of simulating combustion and detonation problems.

With weak (almost negligible) dissipative and good dispersion properties been proven when solving various one- and two-dimensional problems, the CABARET was initially considered as a Perfect LES algorithm. To our knowledge nowadays there are no reported results on the joint implementation of the CABARET scheme and weak compressibility [10] approach when modeling three-dimensional turbulent flows. In this paper, we recall the Taylor-Green vortex flow in order to investigate the scheme dissipative properties analyzing the integral and spectral flow properties. Dealing with integral characteristics of homogeneous turbulence we show, at large, the successful use of weak compressibility formulation and the existence of an intrinsic numerical dissipation mechanism arising especially in the three-dimensional case, as well as the need to reclassify this technique to the group of Implicit LES algorithms [11].

In the following sections we give the problem statement (sect. 2), as well as brief comments about an algorithm implementation (sect. 3), basic relationships for determining the kinetic energy dissipation rate (sect. 4), a concise phenomenological description of the flow evolution (sect. 5), followed by the analysis of integral energy and enstrophy curves (sect. 6). We also discuss spectral characteristics (sect. 7) and spatial correlation functions (sect. 8). In this section we also consider the possible existence of homogeneous or isotropic turbulence in the TGV turbulent decay in terms of turbulent length scales and autocorrelation function. The main results are summarised in the "Conclusion".

2 Problem formulation

Let us consider a periodically extended cubic domain D possessing the dimensions

$$x \in [-\pi L, \pi L], \qquad y \in [-\pi L, \pi L], \qquad z \in [-\pi L, \pi L],$$

where L is a characteristic length scale, with the corresponding initial conditions of the TGV in the domain interior:

$$\begin{aligned}
U &= U_0 \sin\left(\frac{x}{2\pi L}\right) \cos\left(\frac{y}{2\pi L}\right) \cos\left(\frac{z}{2\pi L}\right),\\
V &= -U_0 \cos\left(\frac{x}{2\pi L}\right) \sin\left(\frac{y}{2\pi L}\right) \cos\left(\frac{z}{2\pi L}\right),\\
W &= 0,\\
p &= p_0 + \frac{\rho_0 U_0^2}{16}\left(\cos\left(\frac{x}{\pi L}\right) + \cos\left(\frac{y}{\pi L}\right)\right)\\
&\quad \times \left(\cos\left(\frac{z}{\pi L}\right) + 2\right), \quad p_0 = 0,
\end{aligned} \tag{1}$$

complemented in our case with an equation of state for a weakly compressible fluid:

$$\rho = p/c^2 + \rho_0,$$

wherein c and ρ_0 stand for sound speed and reference density. It is worth noting that the initial conditions for the velocities are divergent as they satisfy the solenoidity relation $\nabla \cdot \boldsymbol{V} = 0$. From the physical standpoint periodic boundary conditions pose an unbounded region filled with a system of identical vortices.

The Taylor-Green vortex is the simplest example of an initially plane flow, in which self-excited vortex stretching occurs with simultaneous three-dimensional velocity field generation.

Further on, Reynolds number will be determined basing on the characteristic length scale

$$\mathrm{Re} = U_0 \rho_0 L / \mu_0. \tag{2}$$

The problem is solved for several Reynolds numbers

$$\mathrm{Re} = 100, 280, 1600, 4000,$$

according to the choice made in [12].

Computational grids have an equal number of cells in three orthogonal directions

$$n_{\mathrm{X}} \times n_{\mathrm{Y}} \times n_{\mathrm{Z}} = 64^3\ (1),\ 128^2\ (2),\ 256^3\ (3).$$

Grid (3) is considered [6] as a lower boundary of the grid range necessary for the correct vortex structures resolution when simulating the vortex decay numerically ($\mathrm{Re} = 1600$); therefore, in this study, we use it to elucidate the question of grid convergence.

Let us estimate the number of grid cells for a good resolution of the smallest scales of homogeneous isotropic turbulence in the three-dimensional case ($\mathrm{Re} = 1600$) as

$$N \approx \mathrm{Re}^{9/4} \approx 16 \times 10^6.$$

Contrary to model problems (such as TGV decay) [5], for real flows the similar estimate yields for an aircraft flow ($\mathrm{Re} \approx 2 \times 10^7$) $N \approx 2 \times 10^{16}$ and for commonly encountered geophysical flows ($\mathrm{Re} \approx 10^{20}$) $N \approx 10^{45}$, that makes impossible a direct numerical simulation (DNS) of these problems.

In the series of calculations all characteristic parameters (U_0, t_0, M), except for the Reynolds number, were kept constant. The three-dimensional implementation of the algorithm is a further development of the two-dimensional version [13–16] of the weak compressibility approximation. A decomposition of the computational domain by planes $z = \mathrm{const}$ was used when parallelizing the algorithm for multiprocessor computers. The calculations were performed on several computing machines at JIHT of RAS, JSCC of RAS and MIPT DPC.

When performing calculations in the hybrid mode (MPI with OpenMP) two additional flat layers of cells are added at the z-axis boundaries of the main grid.

3 Numerical method

The CABARET (Compact Accurately Boundary Adjusting high-Resolution Technique) scheme was rooted in papers by Goloviznin and Samarskii [17,18], which proposed the three-layer implementation of this scheme for the one-dimensional transport equation and showed that the method is conditionally stable in the range of Courant numbers CFL $\in [0,1]$ and exact for CFL $= 0.5, 1$. Later, they revealed the formal similarity of the first variants of the CABARET scheme to the results of Iserles [19] related to the generalization of the classical Leapfrog scheme for hyperbolic equations. However, these schemes are not equivalent to each other, since the Upwind Leapfrog scheme neither is conservative, nor fits into one space-time cell. Ever since the acronym "CABARET" has been referring to as the double-layer divergent form of the finite-difference approximation transport equations. The balance-characteristic approach for the one-dimensional transport equation [20] later extended to compressible flows and supplemented with the nonlinear flux correction algorithm [21] was a further milestone. The use of the characteristic form of transport equations determined the exact localization of such solution features as shock waves and contact surfaces [22].

Gas dynamic tests approved a remarkable efficiency and accuracy when simulating acoustic and vortex flows. In addition, it was shown that in the case of initial conditions special approximation the scheme developed is monotone [23] and strongly monotone [24] for Courant numbers CFL $\in (0, 0.5)$ and nonmonotone for CFL $\in (0.5, 1)$. To eliminate the scheme nonmonotonicity a binary flux correction was proposed, that is performed inside a single spatial cell of a grid.

Nowadays the two-layer CABARET scheme is widely used to simulate gas dynamics [25], acoustics [8,26], chemically reacting [22,27] and incompressible fluid [28] flows, in which equations are solved in "vorticity-stream function" [29] or "velocity-pressure" formulation [30]. The monotonicity of this approach for one- and two-dimensional problems was also studied in [31,32]. The most complete collection of CABARET implementations can be found in the monograph by Goloviznin *et al.* [33].

As indicated above, the CABARET scheme combines the advantages of conservative and characteristic methods in a monolithic approach, that leads to the use of a double set of variables: the first set ("conservative variables") being average values of physical quantities within a single computing cell [27] belongs to the cell centers, while the second one ("flux variables") corresponds to the centers of the cells faces and is responsible for the data interchange between the cells. Flux variables in boundary cells on a new time layer are determined basing on the boundary conditions. Points related to the cell centers are used to solve equations written in a conservative form:

$$\begin{aligned}
&\frac{\partial \rho}{\partial t} + \frac{\partial \rho u}{\partial x} + \frac{\partial \rho v}{\partial y} + \frac{\partial \rho w}{\partial z} = 0,\\
&\frac{\partial \rho u}{\partial t} + \frac{\partial \rho u^2}{\partial x} + \frac{\partial \rho uv}{\partial y} + \frac{\partial \rho uw}{\partial z} + \frac{\partial p}{\partial x} = \Lambda_u U,\\
&\frac{\partial \rho v}{\partial t} + \frac{\partial \rho uv}{\partial x} + \frac{\partial \rho v^2}{y} + \frac{\partial \rho vw}{\partial z} + \frac{\partial p}{\partial y} = \Lambda_v V,\\
&\frac{\partial \rho w}{\partial t} + \frac{\partial \rho uw}{\partial x} + \frac{\partial \rho vw}{y} + \frac{\partial \rho w^2}{\partial z} + \frac{\partial p}{\partial z} = \Lambda_w W.
\end{aligned} \tag{3}$$

The right-hand side of the inhomogeneous momentum transport equations in (3) is also written in a divergent form regardless the compressibility:

$$\begin{aligned}
\Lambda_u U &= \left(\frac{\partial \mu\, q_x^u}{\partial x} + \frac{\partial \mu\, q_y^u}{\partial y} + \frac{\partial \mu\, q_z^u}{\partial z} \right),\\
\Lambda_v V &= \left(\frac{\partial \mu\, q_x^v}{\partial x} + \frac{\partial \mu\, q_y^v}{\partial y} + + \frac{\partial \mu\, q_z^v}{\partial z} \right),\\
\Lambda_w W &= \left(\frac{\partial \mu\, q_x^w}{\partial x} + \frac{\partial \mu\, q_y^w}{\partial y} + \frac{\partial \mu\, q_z^w}{\partial z} \right),
\end{aligned} \tag{4}$$

where $q_x^u, q_y^u, q_z^u, q_x^v, q_y^v, q_z^v, q_x^w, q_y^w, q_z^w$ are velocity gradient tensor components.

Flux variables are used to solve equations in the characteristic form:

$$\begin{aligned}
&\frac{\partial I_k^x}{\partial t} + \lambda_k^x \frac{\partial I_k^x}{\partial x} = G_k^x, \quad \frac{\partial I_k^y}{\partial t} + \lambda_k^y \frac{\partial I_k^y}{\partial y} = G_k^y,\\
&\frac{\partial I_k^z}{\partial t} + \lambda_k^z \frac{\partial I_k^z}{\partial z} = G_k^z, \quad k = 1-4,
\end{aligned} \tag{5}$$

where $I_k^{x,y,z}$ are Riemann's invariants, $\lambda_k^{x,y,z}$ —characteristic numbers and $G_k^{x,y,z}$— the right-hand side terms of transport equations, originating from characteristic form reduction procedure. Accounting for the weak compressibility approximation these invariants and their characteristic numbers in the three-dimensional case are:

$$\begin{aligned}
I_1^x &= c \ln(p + c^2 \rho_0) + u,\\
I_2^x &= -c \ln(p + c^2 \rho_0) + u,\\
I_3^x &= v, \qquad I_4^x = w,
\end{aligned} \tag{6}$$

$$\begin{aligned}
I_1^y &= c \ln(p + c^2 \rho_0) + v,\\
I_2^y &= -c \ln(p + c^2 \rho_0) + v,\\
I_3^y &= u, \qquad I_4^y = w,
\end{aligned} \tag{7}$$

$$\begin{aligned} &I_1^z = c\ln(p + c^2\rho_0) + w,\\ &I_2^z = -c\ln(p + c^2\rho_0) + w,\\ &I_3^z = u, \qquad I_4^z = v, \end{aligned} \tag{8}$$

$$\begin{aligned} &\lambda_1^x = u + c, \qquad \lambda_2^x = u - c, \qquad \lambda_{3,4}^x = u,\\ &\lambda_1^y = v + c, \qquad \lambda_2^y = v - c, \qquad \lambda_{3,4}^y = v,\\ &\lambda_1^z = w + c, \qquad \lambda_2^z = w - c, \qquad \lambda_{3,4}^z = w. \end{aligned} \tag{9}$$

Invariants (6)–(8) are transferred in crosswise directions according to the values of the characteristic numbers (9) and determined by flux variables at the arbitrary time step. The use of the weak compressibility approximation allows to avoid solving the Laplace equation for pressure, and it not only changes the $p = p(\rho)$ function, but also the invariants form, and the algorithm at the extrapolation stage.

It should be noted that, in effect, conservative variables are ρ, ρu, ρv, ρw however, using the terms "conservative" and "flux" variables we follow the originator's terminology encountered in published papers. Conservative and flux variables are interrelated by interpolation only at the initial step. At the subsequent steps they are calculated independently and cannot be obtained directly from each other.

The boundary conditions are set in terms of local Riemann's invariants. In case of periodic boundaries the values of the invariant I_1^∞ determined from the boundary conditions and I_2 delivering information from the domain interior are used to calculate flux variables on the lower and left boundaries while for upper and right borders the pair I_1, I_2^∞ is used. Flux variables include a few mesh sets according to the dimensionality of space and are calculated independently.

To ensure a robust calculation via the explicit scheme, the Courant number CFL $= 0.15$ corresponding to the stability range was used.

A general description of the CABARET numerical method consists of several stages which are: a predictor stage (i), when intermediate conservative variables are calculated via equations in a conservative form; an extrapolation stage (ii), when flux variables on a temporary time layer using linear extrapolation are obtained. Conservative variables on the new time layer are calculated at the corrector stage (iii) by virtue of conservative form equations. As a detailed treatment of the algorithm is rather lengthy, we address the interested reader to the papers [25,13].

4 Basic integral relations

Turbulent evolution of TGV is predominantly studied at the benchmark Reynolds number Re $= 1600$, while the grid convergence analysis is based on the integral kinetic energy

$$E = \frac{1}{2\rho_0 U_0^2 (2\pi L)^3} \iiint_D \rho(U^2 + V^2 + W^2)\,\mathrm{d}x\,\mathrm{d}y\,\mathrm{d}z, \tag{10}$$

the kinetic energy dissipation rate (KEDR)

$$\varepsilon = -\frac{\mathrm{d}E}{\mathrm{d}t}\,, \tag{11}$$

and the enstrophy

$$\zeta = \frac{t_0^2}{(2\pi L)^3} \iiint_D \boldsymbol{\omega}^2/2\,\mathrm{d}x\,\mathrm{d}y\,\mathrm{d}z, \tag{12}$$

rather than on the direct error calculation for velocity and vorticity fields.

For an incompressible fluid, the enstrophy is proportional to the dissipation rate of the kinetic energy [34]:

$$\varepsilon_1 = -2\frac{\mu}{\rho_0}\frac{t_0}{(2\pi L)^2}\zeta, \tag{13}$$

whereas for the compressible flow KEDR is determined by the sum of two components determined by the deviatorial part of the strain rate tensor:

$$\varepsilon_2 = 2\frac{\mu t_0}{\rho_0 U_0^2 (2\pi L)^3} \iiint_D S_{ij}S_{ij}\,\mathrm{d}x\,\mathrm{d}y\,\mathrm{d}z, \tag{14}$$

wherein tensor convolution yields

$$\begin{aligned} S_{ij}S_{ij} = {} & \left(\frac{\partial U}{\partial x}\right)^2 + \left(\frac{\partial V}{\partial y}\right)^2 + \left(\frac{\partial W}{\partial z}\right)^2\\ & + \frac{1}{2}\left(\frac{\partial U}{\partial y} + \frac{\partial V}{\partial x}\right)^2 + \frac{1}{2}\left(\frac{\partial U}{\partial z} + \frac{\partial W}{\partial x}\right)^2\\ & + \frac{1}{2}\left(\frac{\partial V}{\partial z} + \frac{\partial W}{\partial y}\right)^2, \end{aligned} \tag{15}$$

and by compressibility effects. To estimate the influence of the latter on turbulence, we can calculate the dissipation rate from pressure dilatation:

$$\varepsilon_3 = -\frac{t_0}{U_0^2}\frac{1}{\rho_0(2\pi L)^3} \iiint_D p\nabla\cdot\boldsymbol{V}\,\mathrm{d}x\,\mathrm{d}y\,\mathrm{d}z. \tag{16}$$

The integration is performed by a trapezoidal method which, due to the arrangement of points in the cell centers, is reduced to a simple summation.

5 General flow description

TGV is a simple example of a flow allowing to keep track of the mechanisms of turbulent decay, generation of small vortices and an enhancement of dissipation due to vortex tubes deformation. Depending on Re, various flow regimes are observed, in particular, the decay of a single vortex at Re $= 100, 280$ is laminar, and the formation of a random vorticity field does not occur. Figure 1 shows an example of such a decay at Re $= 100$, where the vorticity component ω_z is represented by two groups of level surfaces marked with blue ($\omega_z \leq -0.2$) and red colors ($\omega_z \geq 0.2$).

For sufficiently large Reynolds numbers, the evolution of the vortex has two stages [35]: at the first one, the effect

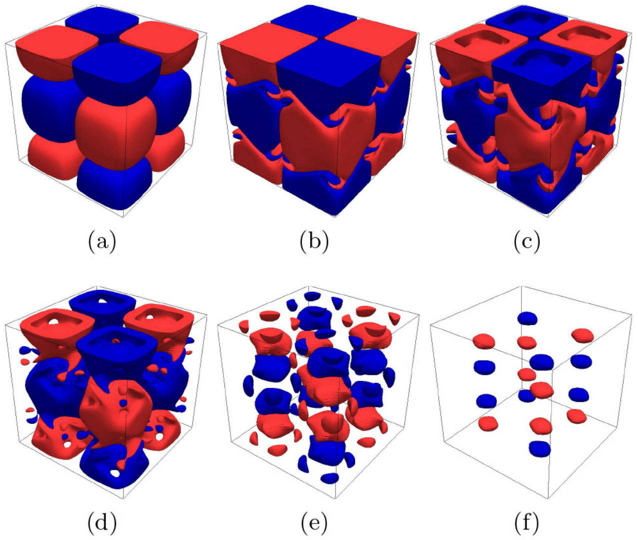
(a) (b) (c)

(d) (e) (f)

Fig. 1. The vorticity field evolution in the case of laminar vortex decay (Re $= 100$) in the range $\omega_z \leq -0.2 \cup \omega_z \geq 0.2$ at different time instants: (a) $t = 0$, (b) $t = 5$, (c) $t = 10$, (d) $t = 15$, (e) $t = 20$, (f) $t = 25$.

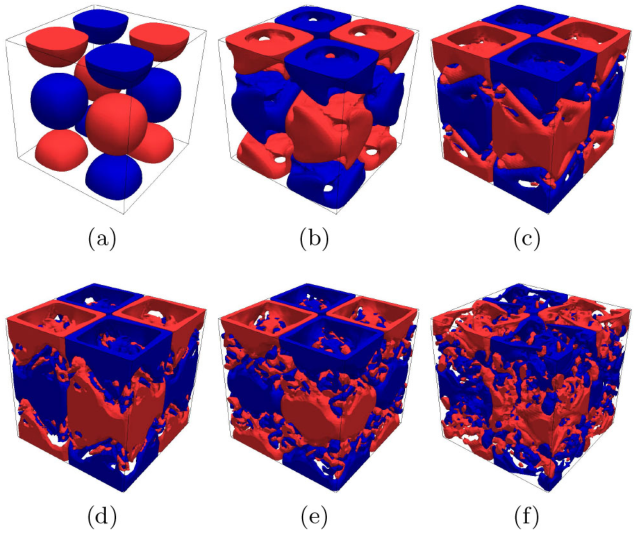
(a) (b) (c)

(d) (e) (f)

Fig. 2. The vorticity field in the case of turbulent decay of TGV at the highest number Re $= 4000$ in the range $\omega_z \leq -0.7 \cup \omega_z \geq 0.7$ at different instants of time: (a) $t = 0$, (b) $t = 3$, (c) $t = 5$, (d) $t = 7$, (e) $t = 9$, (f) $t = 12$.

of viscosity is negligibly small and small-scale structures are regular and laminar. The laminar inviscid evolution at $t \approx 3$ (fig. 2(b)) leads to vortices roll-up at $t \approx 5$ (fig. 2(c)) with subsequent topology changes at $t \approx 7$ (fig. 2(d)). At the second stage the energy dissipation plays a key role, as well as the diffusion processes due to the existence of viscosity. In addition, regions of active energy dissipation are formed, that reaches its maximum at the late part of the "viscous stage" ($t \approx 8.5$). At $t \approx 9$ (see fig. 2(e)), the coherent structures are destroyed leading to the developed turbulent flow, which begins to decay at time $t > 12$ (see fig. 2(f)). It is believed that areas with strong vorticity correspond to vortex tubes [35], while the domains of strong energy dissipation are associated with sheet-like structures.

As the eventual result of both laminar and turbulent decay of the vortex is a resting medium, the TGV flow should be treated in terms of spatial rather than temporal chaos [3], since a nontrivial attractor in the state space does not exist at $t \to \infty$. These considerations allow us to justify the application of spatial averaging when calculating correlation functions (sect. 8) for large Reynolds numbers.

6 The analysis of integral energy and enstrophy curves

As previously noted the major approach of assessing the accuracy of TGV modeling is to compare the integral curves of kinetic energy (10), its dissipation rate calculated via different fomulae (11)–(14), (16) and enstrophy at various Reynolds numbers and grid resolution.

The KEDR curves obtained directly using (10), (11) for different Reynolds numbers are shown in fig. 3. Besides ε one can pay attention to the behavior of the relative error ϵ_{grid} concerned with grid convergence and determined by

$$\epsilon_{\varepsilon,\mathrm{grid}} = \frac{|\varepsilon_{i,256} - \varepsilon_{i,k}|}{\varepsilon_{i,256}}, \qquad (17)$$

where $\varepsilon_{i,256}$ and $\varepsilon_{i,k}$ stand for the results obtained on the finest grid 256^3 and k^3, $k = 64, 128$ correspondingly.

In case of laminar decay at Re $= 100$ while the grid is refined, the maximum discrepancy between the results of the CABARET scheme and the reference values [12] corresponds to the maximum of KEDR at $t \approx 5$. The curves obtained at grid (1) (red line in fig. 3(a)) and grid (3) approximately coincide (black line in fig. 3(a)), while the graph for grid (2), colored in blue, is somewhat lower, completely coinciding with the reference values [4], and Quasigasdynamic (QGD) approach [12] overestimates ε.

A similar behavior is observed at Re $= 280$ (fig. 3(b)), where the discrepancy between the results of CABARET calculation series is almost negligible, while the QGD approach yields 3% overestimate.

Turning to turbulent vortex decay (Re $= 1600$) shows that for the most detailed grid in all sections of the curve $\varepsilon = \varepsilon(t)$ (fig. 3(c)) the results of the CABARET scheme show a good agreement with a model solution [36], obtained by the spectral method (the bright green curve). For the largest Reynolds number Re $= 4000$, grid refinement increases ε (see fig. 3(d)) in the turbulence developing region (due to better resolution of vortex formations) and decreases it at the stage of turbulent decay as the dissipation proceeds faster.

The close agreement of curves $\varepsilon = \varepsilon(t)$ at Re $= 1600$ and Re $= 4000$ is probably due to approaching to a "limiting" dissipative process independent of the Reynolds number [37].

The previous analysis should be extended by considering the set of integral enstrophy curves $\zeta = \zeta(t)$ (see

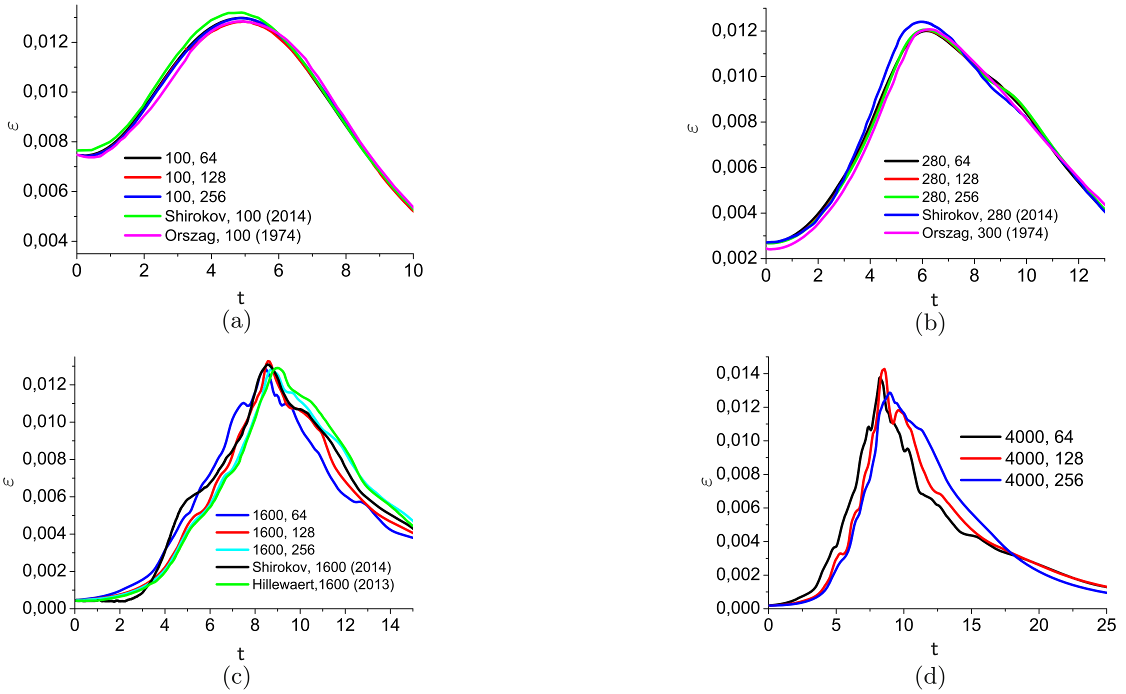

(a) (b) (c) (d)

Fig. 3. The dissipation rate calculated directly on the sequence of refined grids for different Reynolds numbers compared with the results of [12,4]: (a) Re = 100; (b) Re = 280; (c) Re = 1600; (d) Re = 4000.

fig. 4), which allow to make important conclusions about the quality of the numerical method employed.

The law $\zeta = \zeta(t)$ is analyzed more rarely, however, it shows the necessity of a more detailed grid resolution within the laminar decay, as ε_1 depends on the quality of vortex structures modeling.

In the case of laminar decay the maximum relative error calculated in a similar way as (17) falls in the region of the maximum dissipation rate. The rapid decline of kinetic energy at the peak of dissipation is due to the excitation of inviscid instability and coincides with the peak of enstrophy [6].

Proceeding to Re = 1600 and comparing the results at the finest grid to simulation [38] performed on 512^3 cells (see fig. 4(b)) it is easy to verify that grid (3) is still insufficient. In fact, the gain in the accuracy increase due to simple mesh refinement appears to be more significant compared to searching through more and more sophisticated numerical methods. A similar situation is observed at Re = 4000, however, the loss of solution accuracy already takes place on the finest grid, since the main peak of enstrophy is not so clear (compare fig. 4(b) and (c)). Figure 4(d) presents a summary plot characterizing the enstrophy enhancement during the transition to the developed turbulent regime; the maximum relative multiplication $\zeta_{\max}/\zeta_0$ is shown in table 1 (grid (3)).

The difference between KEDR ε computed directly and determined from enstrophy ζ data using the relation (13), which is valid for an incompressible fluid at any time of the flow development [34] (see the set of curves in fig. 5) allows to make decisive conclusions about the characteristics of the numerical method.

Table 1. The maximum growth of the integral enstrophy reduced by the initial values.

Re	100	280	1600	4000
$\zeta_{\max}/\zeta_0$	1.73	4.46	21.57	34.16

On coarse grids KEDR obtained from enstrophy ε_1 is substantially lower than the results of direct calculation. Thus, the dissipative mechanism due to the expansion of the vortex tubes does not correspond to the energy loss processes in simulation being a consequence of the additional numerical dissipation. The modeling approach, in which the dissipation existing in numerical schemes provides an opportunity to neglect subgrid models of small-scale dissipation, was called implicit LES (ILES). When the turbulence is attenuated ($10 < t < 25$), a coarser grid leads to an increased dissipation of the kinetic energy [34]. Calculating the components ε associated with the strain rate tensor ε_2 (fig. 6) and pressure dilatation ε_3 (fig. 7(a)) shows that the main contribution is made by viscous dissipation, and the role of ε_3 is negligibly small, especially when mesh is refined, which provides additional justification for the applicability of the weak compressibility approximation.

At the end of this section let us consider the asymptotic behavior of $E = E(t)$ at the decay stage of turbulent flow, shown in fig. 7(b) for various grids (Re = 1600). The exponent "-1.2" for the time dependence of energy is treated as a characteristic value of decaying turbulence [39]. The law $E \propto t^{-1.2}$ is valid only for a fairly narrow time interval of about $t \sim$ 8–10, which is usually attributed to the

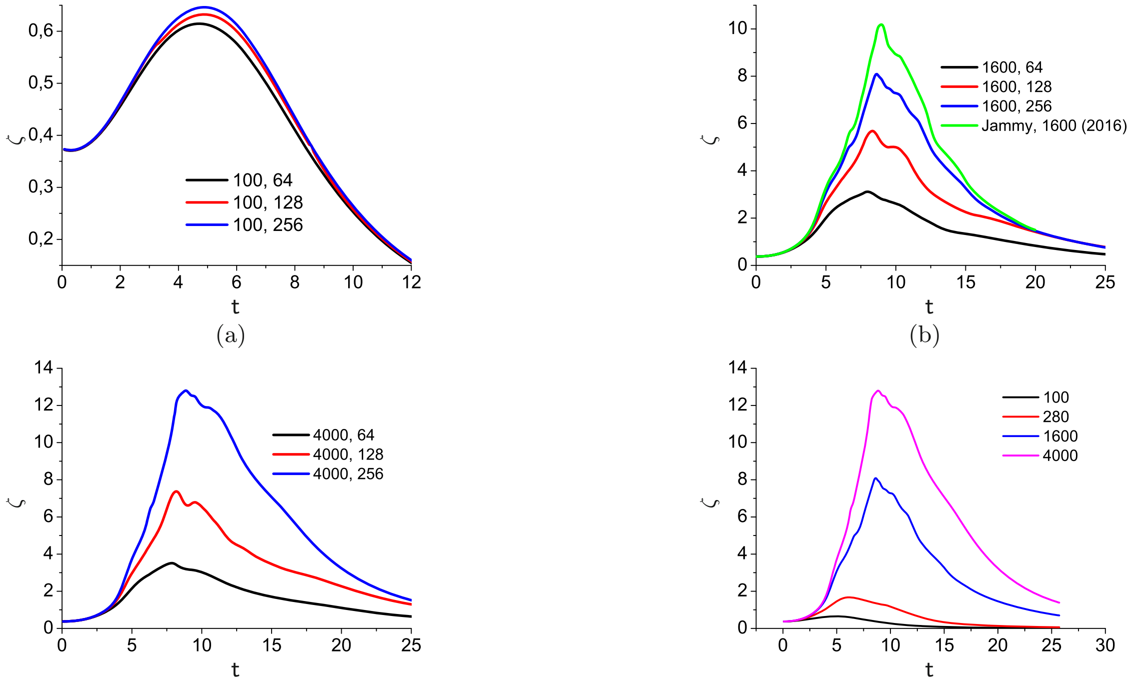

(a) (b)

(c) (d)

Fig. 4. A time variation of integral enstrophy: the convergence of results on a sequence of refined grids for different Reynolds numbers: (a) Re = 100; (b) Re = 1600; (c) Re = 4000; (d) a summary graph for various Reynolds numbers (256^3 grid).

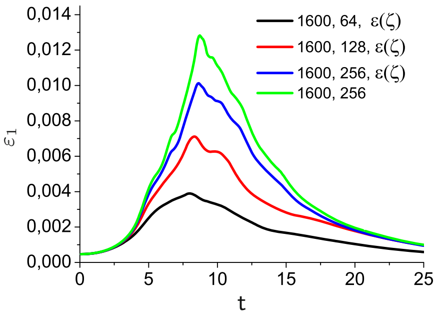

Fig. 5. The dissipation rate calculated on the basis of the enstrophy integral $\zeta = \zeta(t)$ marked in the legend as "$\varepsilon(\zeta)$"; the green curve shows the directly computed ε.

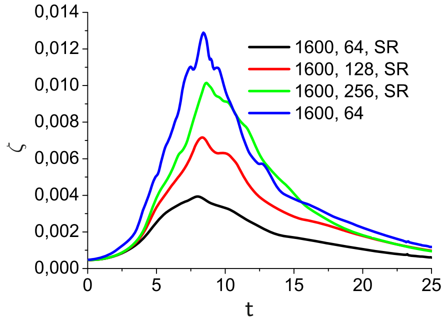

Fig. 6. The dissipation rate calculated on the basis of the strain rate tensor denoted in the legend as "SR"; the blue curve shows the results of direct calculation.

peak of kinetic energy dissipation. Immediately after this the decline actually falls to $E \propto t^{-2}$. The transition to the exponent "-2" is probably related to the saturation of energy-containing scales, which reflects the fact that the existence of vortices larger than the periodic region is impossible [40].

7 Fourier spectra

Contrary to spectral numerical methods, which can use several thousand expansion terms in one direction reaching very high accuracy, the finite-difference methods are limited to a much smaller value. The usual methods in this case are linear or logarithmic averaging over spherical shells. In this case, the substantial difference between the values of even and odd wave numbers k plays a role, which, possibly, is a consequence of the series truncation of the spectral expansion and the special symmetry of the vortex [3]. Such averaging leads to underestimated amplitude values. In addition, the procedure of simple summation of harmonics with different amplitudes is performed without any sustainable argumentation.

As a result, in order to obtain sufficiently detailed spectra, it is necessary to reduce the thickness of the spherical shells being used for averaging. So we have to utilize very thin spherical shells yielding "shaky" spectra. To overcome this drawback a special averaging procedure was employed [41]. Additionally, Intel MKL library was used to implement a three-dimensional Fourier transform.

The obtained Fourier spectra of the developed turbulent flow (see fig. 8) correspond to the maximum of

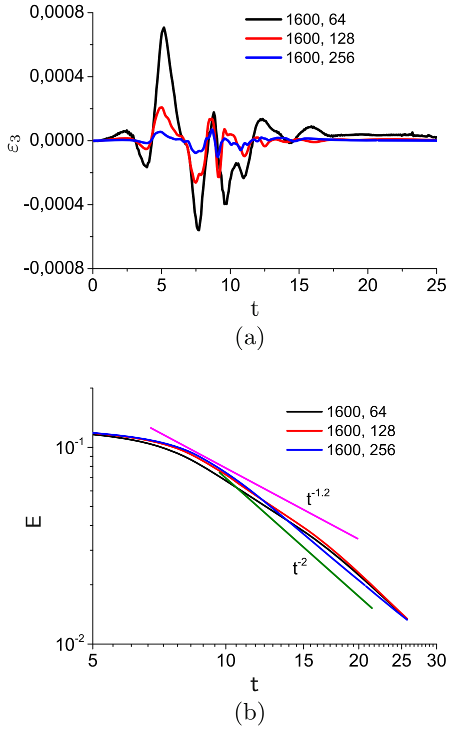

(a)

(b)

Fig. 7. (a) The dissipation rate ε_3 due to the pressure dilatation; (b) the time dependence of kinetic energy E calculated on a sequence of grids, the magenta line indicates the slope of the asymptotics $t^{-1.2}$ and the green one asymptotics t^{-2}.

dissipation rate at $t \approx 8.5$. A comparison of energy spectra from ref. [12] with the results obtained using the CABARET scheme is shown in fig. 8(a). CABARET spectra seem to yield a better approximation to "$-5/3$" asymptotics, but, on the other hand, a slight steepening of spectral tails confirms an assumption of numerical dissipation. According to time evolution of spectra (see fig. 8(b)) when the flow develops $5 < t < 10$, the spectral curves approach the asymptotics "$-5/3$".

At the decay stage $t > 10$, the negative slope of the spectra is amplified, although the roll-off should affect only the spectrum tail, that is not observed due to insufficient spectral resolution. Conversely, in the case under consideration, steepening covers almost the entire wave number interval. At Re $= 4000$, the mesh refinement (fig. 8(c)) slightly extends the interval of "$-5/3$" asymptotics.

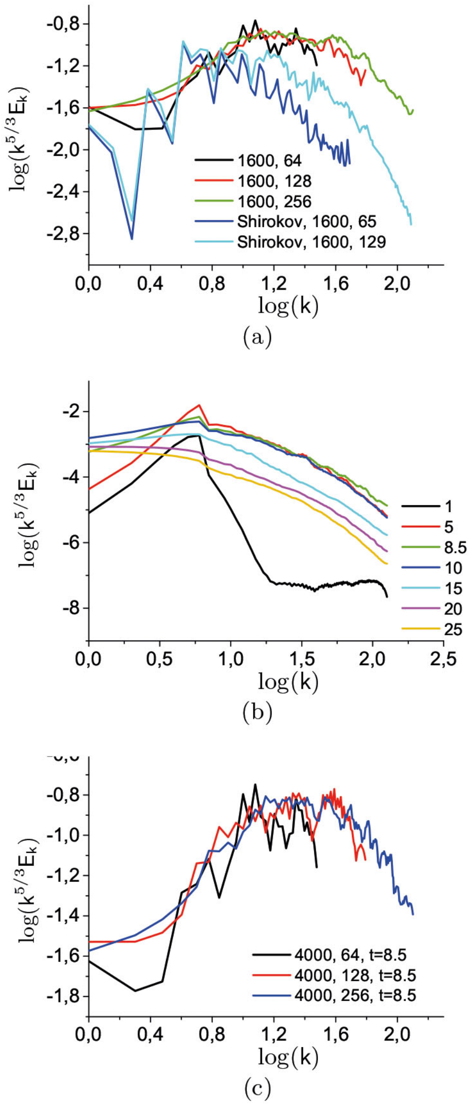

(a)

(b)

(c)

Fig. 8. (a) Flow energy spectra at time $t = 8.5$, (Re $= 1600, 256^3$) compared to QGD approach [12]; (b) time evolution of energy spectra (Re $= 4000, 256^3$); (c) similar spectra at $t = 8.5$, Re $= 4000, 256^3$.

8 Correlation functions

Certain sections of the kinetic energy spectrum corresponding to the "$-5/3$" asymptotics for isotropic turbulence can be misleading with respect to its general characteristics. In particular, we can calculate a longitudinal autocorrelation function $Q_{ii}(r) = \langle U(x,y,z)U(x+r,y,z)\rangle$ and a third-order velocity correlation function (or tensor) $S_{iii}(r) = \langle U(x,y,z)^2 U(x+r,y,z)\rangle$, which in the case of isotropic turbulence take the form $Q_{ii}(r) = \langle u^2\rangle f(r)$ and $S_{iii}(r) = \langle u^2\rangle^{3/2} K(r)$, where $\langle u^2\rangle = Q_{ii}(0)$ is the mean square of the turbulent fluctuations, $f(r)$ is the "classical" longitudinal velocity correlation function, $K(r)$ is the longitudinal triple correlation function (in the notations of Davidson [42]). The function $f(r)$ is positive, while $K(r)$ is negative, but they both tend to zero at infinite distance of the correlation points from each other.

Using $K(r)$, one can find the spectral kinetic energy transfer

$$T(k) = \frac{k}{\pi}\int_0^\infty \frac{1}{r}\frac{\partial}{\partial r}\frac{1}{r}\frac{\partial}{\partial r}\left[r^4 u^3 K(r)\right]\sin(kr)\mathrm{d}r \qquad (18)$$

and flux

$$\mathit{\Pi}_E(k) = -\int_0^k T(k')\mathrm{d}k' \qquad (19)$$

functions involved in a spectral analog of the Karman-Howarth equation.

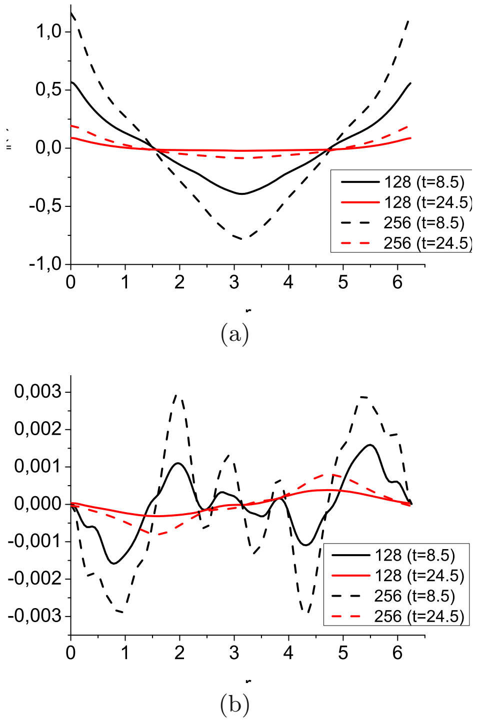

Fig. 9. The autocorrelation function $Q_{ii}(r)$ (a) and third-order velocity correlation function $S_{iii}(r)$ (b) at the instant of the maximum dissipation rate $t = 8.5$ (black lines), as well as the decay stages of turbulence at $t = 24.5$ (red lines). Solid curves show results on grid 128^3 and dashed ones those on the grid 256^3.

The calculation of the distance r between points was carried out regardless of the spatial periodicity, that is, the existence of the nearest point image.

Considering results of [43] and our own calculations of $Q_{ii}(r)$ and $S_{iii}(r)$, shown in fig. 9, at the instant of the KEDR maximum $t \approx 8.5$ and also at the end of the calculation $t \approx 24.5$, one can inspect a decisive influence of periodic initial conditions on the shape of the autocorrelation function. It approaches the starting value as the distance between the correlation points increases to the domain size. According to the autocorrelation curves correlation and periodicity are preserved in the whole computational domain, that differs significantly from the properties of isotropic turbulence.

Changing the maximum distance r between correlation points when calculating $Q_{ii}(r)$ and $S_{iii}(r)$ as $r = 4\lambda_\tau$, $6\lambda_\tau$, $8\lambda_\tau$, πL, $2\pi L$ does not influence the functions behaviour. The autocorrelation curve obtained on the finest grid 256^3 is even sharper because single-point rms pulsations are stronger, and the anticorrelation in the center of the region is greater. This effect is also observed at the turbulence decay stage.

Thus, the results obtained differ from the actual properties of isotropic turbulence where the autocorrelation function $Q_{ii}(r) \to 0$, if $r \to \infty$, so the turbulence observed in the Taylor-Green vortex decay is essentially nonisotropic.

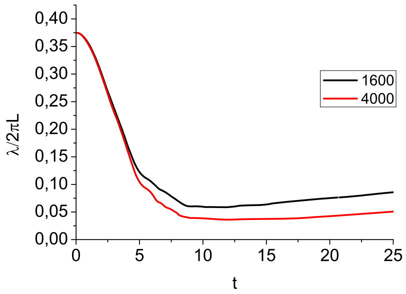

Fig. 10. Temporal dependence of the Taylor microscale reduced to domain size, calculated on the grid 256^3.

These considerations can be explained when estimating the characteristic scales of turbulence, employing the scale relations for the ideal isotropic case, such as the connection between the Taylor microscale λ_τ and the integral scale l. Consequently, we obtain:

$$\lambda_\tau / l \sim \sqrt{\frac{15}{\mathrm{Re}}} = \sqrt{\frac{15}{1600}} \approx 0.096. \tag{20}$$

Thus, the scales differ by almost an order of magnitude. Under the same assumption, we calculate the Taylor microscale by the formula

$$\lambda_\tau{}^2 = \frac{15\nu\langle u^2\rangle}{\varepsilon}, \quad \langle u^2\rangle = E/3. \tag{21}$$

This quantity reduced by domain size is presented in fig. 10 for Re = 1600 and Re = 4000, its values should be considered from the instant of maximum dissipation rate $t \geq 9$ when a developed turbulent flow is generated. The $\lambda_\tau = \lambda_\tau(t)$ dependence for Re = 1600 shows that $\hat{\lambda}_\tau = \lambda_\tau / 2\pi L \sim 0.07$ at the stage of turbulence decay which is in general agreement with the dimensionless (20).

Following the observations of Davidson [42] one notes that in order to obtain satisfactory spectral characteristics in the range of small and medium wave numbers, it is necessary to require $2\pi L > 20l \to 40l$. In this case we obtain

$$\lambda_\tau / l \sim 0.096, \tag{22}$$

$$\lambda_\tau / (2\pi L) \sim 0.07, \tag{23}$$

that yields

$$l/(2\pi L) \sim \frac{0.07}{0.096} \sim 0.7. \tag{24}$$

Thus, the presented results cannot correspond to the theory of isotropic turbulence as the integral scale l is comparable to the size of computational domain, probably because of the nature of the problem formulated.

To confirm the coherence between the areas of strong vorticity and rarefaction we calculate the spatial correlation function for the pressure p variables and squared vorticity $\boldsymbol{\omega}^2 = \omega_x^2 + \omega_y^2 + \omega_z^2$:

$$R_{pe} \frac{\langle p\,\boldsymbol{\omega}^2\rangle}{\sqrt{\langle p^2\rangle}\sqrt{\langle(\boldsymbol{\omega}^2)^2\rangle}}, \tag{25}$$

where

$$\langle p\,\boldsymbol{\omega}^2\rangle = \frac{t_0^2}{c^2\rho_0(2\pi L)^3}\iiint_D p\left(\boldsymbol{\omega}^2\right)^2 \mathrm{d}x\,\mathrm{d}y\,\mathrm{d}z, \quad (26)$$

$$\langle p^2\rangle = \frac{1}{c^4\rho_0(2\pi L)^3}\iiint_D p^2\,\mathrm{d}x\,\mathrm{d}y\,\mathrm{d}z, \quad (27)$$

$$\left\langle\left(\boldsymbol{\omega}^2\right)^2\right\rangle = \frac{t_0^4}{(2\pi L)^3}\iiint_D (\boldsymbol{\omega}^2)^2\,\mathrm{d}x\,\mathrm{d}y\,\mathrm{d}z. \quad (28)$$

In addition, one can also examine the correlation between instantaneous spatial deviations of p', $(\boldsymbol{\omega}^2)'$:

$$p = \bar{p} + p', \quad (29)$$

$$\bar{p} = \frac{1}{(2\pi L)^3}\iiint_D p\,\mathrm{d}x\,\mathrm{d}y\,\mathrm{d}z, \quad (30)$$

$$\boldsymbol{\omega}^2 = \overline{\boldsymbol{\omega}^2} + \left(\boldsymbol{\omega}^2\right)', \quad (31)$$

$$\overline{\boldsymbol{\omega}^2} = \frac{1}{(2\pi L)^3}\iiint_D \boldsymbol{\omega}^2\,\mathrm{d}x\,\mathrm{d}y\,\mathrm{d}z, \quad (32)$$

$$R_{p'e'}\frac{\langle p'\,(\boldsymbol{\omega}^2)'\rangle}{\sqrt{\langle(p-\bar{p})^2\rangle}\sqrt{\langle(\boldsymbol{\omega}^2-\overline{\boldsymbol{\omega}^2})^2\rangle}}, \quad (33)$$

where

$$\langle p'\,(\boldsymbol{\omega}^2)'\rangle = \frac{t_0^2}{c^2\rho_0(2\pi L)^3}\iiint_D p'\left(\boldsymbol{\omega}^2-\overline{\boldsymbol{\omega}^2}\right)\mathrm{d}x\,\mathrm{d}y\,\mathrm{d}z, \quad (34)$$

$$\langle p^{2\prime}\rangle = \frac{1}{c^4\rho_0(2\pi L)^3}\iiint_D (p-\bar{p})^2\,\mathrm{d}x\,\mathrm{d}y\,\mathrm{d}z, \quad (35)$$

$$\left\langle\left(\boldsymbol{\omega}^2\right)^2\right\rangle = \frac{t_0^4}{(2\pi L)^3}\iiint_D \left(\boldsymbol{\omega}^2-\overline{\boldsymbol{\omega}^2}\right)^2\mathrm{d}x\,\mathrm{d}y\,\mathrm{d}z. \quad (36)$$

The resultant curve $R_{pe} = R_{pe}(t)$ even obtained on coarse grids (1) and (2) allows to catch the main features of the flow (see fig. 11):

- the values of R_{pe} are negative in the entire time interval, so that the areas of strong vorticity correspond to rarefaction;
- R_{pe} is a strongly nonmonotonic function: there is a loss of field coupling during the laminar decay of TGV at $0 < t < 2.5$, while the anticorrelation increases with vortex roll-up and reaches its minimum at $t \approx 5$. Further, it retains its value in the range (-0.6 ± 0.05) at $5 < t < 11$, when a fully turbulent flow develops. An increase in R_{pe} implying the "rupture" of the correlation at $t \approx 7$ may occur due to structure changes of the vorticity field. With further decay of turbulence $|R_{pe}|$ decreases, so the correlation becomes weaker, that can be caused by both physical and numerical dissipation and also by insufficient grid resolution;
- the same curve for a larger Reynolds number shows a similar dependence. A complete set of curves $R_{pe} = R_{pe}(t)$ on the sequence of refined grids for Re $= 4000$ is shown in fig. 11(b);
- a mesh refinement generally damps the correlation dependence;

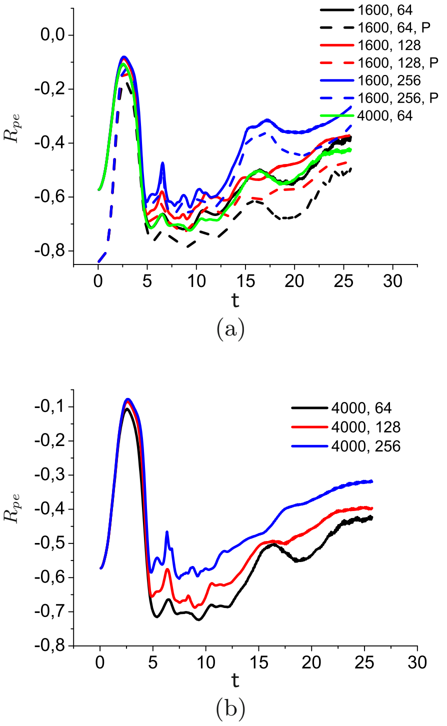

(a)

(b)

Fig. 11. Cross-correlation function of pressure and squared vorticity $R_{pe} = R_{pe}(t)$: (a) Re $= 1600$; (b) Re $= 4000$.

- computing of correlation based on the spatial fluctuations ("pulsations"), *i.e.* a deviation from the spatial mean, shows that anticorrelation $R_{pe} > R_{p'e'}$ increases for coarse grids, nevertheless both approaches yield nearly identical curves for the most detailed grid (3) (solid and dashed blue curves in fig. 11(a)).

The additional flow analysis can be performed using skewness and flatness factors:

$$S_n(r) = (-1)^n\frac{\langle[U(x+r,y,z)-U(x,y,z)]^n\rangle}{\langle[U(x+r,y,z)-U(x,y,z)]^2\rangle^{1/2n}}\,,$$
$$S_n(0) = (-1)^n\frac{\langle(\partial U(x,y,z)/\partial x)^n\rangle}{\langle(\partial U(x,y,z)/\partial x)\rangle^{1/2n}}\,, \quad (37)$$

where $\langle\ \rangle$ in (37) means spatial averaging over the periodic domain. Inspecting these functions depicted in fig. 12 along with the results of Brachet *et al.* [3] one can see that the main contribution is made by the regions in the vicinity of $r = 0$. As the spatial derivative is approximated by finite differences, it follows that $S_n(0) = S_n(2\delta x)$.

The analysis of the grid convergence of the structure function S_3 (see fig. 13) shows that an adequate behavior compared to reference values can be obtained only for the finest grid. Structure functions of various order at $r = 0$ are listed in table 2 along with the reference values [3] indicated in parentheses. It is worth noting that the accuracy of the calculation for the last structure function decreases significantly.

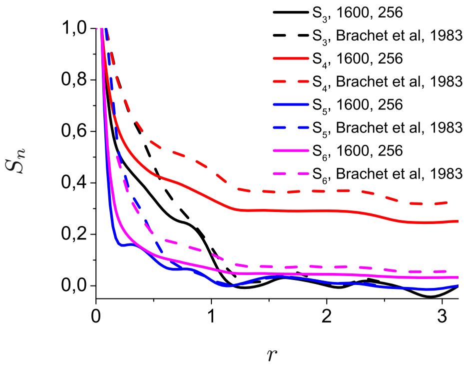

Fig. 12. The dependence of structure functions on the correlation length r; comparison of the obtained data with the reference ones.

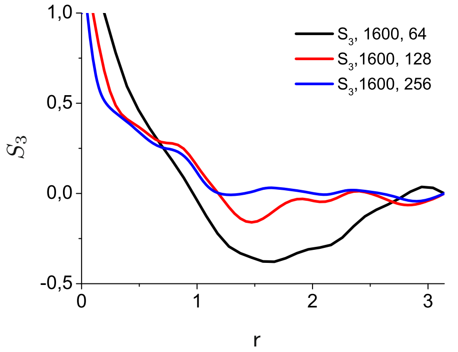

Fig. 13. The structure function S_3 *versus* correlation length r on various grids with Reynolds number $\mathrm{Re} = 1600$.

Table 2. Structure functions S_n of various orders at $r = 0$.

S_3	S_4	S_5	S_6
0.58(0.65)	12.66(10)	23.26(23.1)	459.2(273)

9 Conclusion

The Taylor-Green vortex problem turns out to be a useful benchmark allowing to verify the quality of the numerical method when modeling complicated vortex flows accompanied by the formation of multiscale structures and their nonlinear interaction. The finite-difference explicit second-order accuracy CABARET method is considered in comparison with other numerical approaches such as QGD, spectral and Galerkin methods, which obviously have a superiority when modeling flows in periodic domains. CABARET scheme possessing a considerable versatility, provides a viable alternative to the mentioned approaches in terms of vortex structures resolution both at laminar and turbulent decay and integral parameters calculation. Unfortunately, the numerical dissipation mechanism does not exactly conform to the real physical process, as on coarse meshes the values of kinetic energy dissipation rate ε_1 obtained from enstrophy are substantially lower than the results of direct differencing. Thus, the method used in the present study should be referred to the group of ILES methods expecting that its dissipative properties enable to omit the subgrid models for underresolved scales. As concerns the vortex structure resolution, the transition to smaller grids can be more efficient as compared to the use of sophisticated high-order accuracy numerical methods.

Considering turbulent decay, one can recognize the influence of periodic boundary conditions being artificial from the physical point of view, as they determine the law of decrease of turbulent kinetic energy at long evolution times, whereas according to classical concepts such a turbulent flow should forget its initial state. The flow energy spectrum at the instant of the maximum dissipation rate approaches "−5/3" asymptotics, while an appreciable damping of the high-frequency spectral range takes place. As the Taylor-Green vortex possesses a spatially chaotic vorticity field, it can be treated in terms of spatial correlation functions that allows to investigate the general anticorrelation between domains of strong vorticity and rarefaction.

The authors express their deep gratitude to Data Processing Center of Moscow Institute of Physics and Technology, Joint Supercomputer Center of Russian Academy of Sciences, and Joint Institute for High Temperatures of Russian Academy of Sciences for providing access to computing resources. We are also grateful to our colleagues Vladislav A. Panov, Alexey A. Kuroedov and Nikita G. Misuna for their useful comments on the paper manuscript. The work was supported by the Russian Science Foundation (project No. 14-50-00124).

Author contribution statement

YMK developed numerical scheme program implementation and carried out the calculations. EES inspired and guided problem solving and results analysis. Both YMK and EES were involved in the preparation of the manuscript.

References

1. G.I. Taylor, A.E. Green, Proc. R. Soc. London, Ser. A **158**, 499 (1937).
2. S. Goldstein, Lond. Edinb. Dublin. Philos. Mag. **30**, 85 (1940).
3. M. Brachet, D. Meiron, S. Orszag, B. Nickel, R. Morf, U. Frisch, J. Fluid Mech. **130**, 411 (1983).
4. S. Orszag, *Numerical simulation of the Taylor-Green vortex* (Springer Berlin Heidelberg, Berlin, Heidelberg, 1974) pp. 50–64.
5. L. Berselli, J. Math. Fluid Mech. **7**, S164 (2005).
6. D. Drikakis, C. Fureby, F.F. Grinstein, D. Youngs, J. Turbul. **8**, N20 (2007) DOI: `https://doi.org/10.1080/14685240701250289`.
7. E.V. Koromyslov, M.V. Usanin, L.Y. Gomzikov, A.A. Siner, Comput. Contin. Mech. **8**, 24 (2015) (*Utilization of high order DRP-type schemes and large eddy simulation based on relaxation filtering for turbulent gas flow computations in the case of Taylor-Green vortex breakdown*; DOI: `https://doi.org/10.7242/1999-6691/2015.8.1.3`).

8. V. Goloviznin, S. Karabasov, T. Kozubskaya, N. Maksimov, Comput. Math. Math. Phys. **49**, 2168 (2009).
9. C. Tam, J. Webb, J. Comput. Phys. **107**, 262 (1993).
10. N. Taguelmimt, L. Danaila, A. Hadjadj, Flow Turbul. Combust. **96**, 163 (2016).
11. L.G. Margolin, W.J. Rider, F.F. Grinstein, J. Turbul. **7**, N15 (2006).
12. I. Shirokov, T. Elizarova, J. Turbul. **15**, 707 (2014).
13. Y. Kulikov, E. Son, J. Phys.: Conf. Ser. **774**, 012094 (2016).
14. Y. Kulikov, E. Son, Comput. Res. Model. **9**, 881 (2017) DOI: `https://doi.org/10.20537/2076-7633-2017-9-6-881-903`.
15. Y. Kulikov, E. Son, J. Phys.: Conf. Ser. **946**, 012075 (2017).
16. Y. Kulikov, E. Son, Thermophys. Aeromech. **24**, 909 (2017).
17. V. Goloviznin, A. Samarskii, Matem. Mod. **10**, 86 (1998).
18. V. Goloviznin, A. Samarskii, Matem. Mod. **10**, 101 (1998).
19. A. Iserles, IMA J. Numer. Anal. **6**, 381 (1986).
20. V. Goloviznin, S. Karabasov, I. Kobrinskiy, Math. Models Comput. Simul. **15**, 29 (2003).
21. V. Goloviznin, Matem. Mod. **18**, 14 (2006).
22. M. Ivanov, A. Kiverin, S. Pinevich, I. Yakovenko, J. Phys.: Conf. Ser. **754**, 102003 (2016).
23. V. Ostapenko, Matem. Mod. **21**, 29 (2009).
24. V. Ostapenko, Comput. Math. Math. Phys. **52**, 387 (2012).
25. S. Karabasov, V. Goloviznin, AIAA J. **45**, 2801 (2007).
26. V. Semiletov, S. Karabasov, J. Comput. Phys. **253**, 157 (2013).
27. A.V. Danilin, A.V. Solovjev, A.M. Zaitsev, Numer. Methods Program. **18**, 1 (2017) (*A modification of the CABARET scheme for numerical simulation of one-dimensional detonation flows using a one-stage irreversible model of chemical kinetics*).
28. S. Karabasov, P. Berloff, V. Goloviznin, Ocean Model. **30**, 155 (2009).
29. V. Glotov, V. Goloviznin, Math. Models Comput. Simul. **4**, 144 (2012).
30. V. Glotov, V. Goloviznin, Comput. Math. Math. Phys. **53**, 721 (2013).
31. O. Kovyrkina, V. Ostapenko, Math. Models Comput. Simul. **5**, 180 (2013).
32. O. Kovyrkina, V. Ostapenko, Dokl. Math. **91**, 323 (2015).
33. V. Goloviznin, M. Zaytsev, S. Karabasov, I. Korotkin, *Novel Algorithms of Computational Hydrodynamics for Multicore Computing* (Moscow University Press, 2013).
34. J. DeBonis, *Solutions of the Taylor-Green Vortex Problem Using High-Resolution Explicit Finite Difference Methods*, in *Aerospace Sciences Meetings* (American Institute of Aeronautics and Astronautics, 2013) p. 0382.
35. M. Brachet, Fluid Dyn. Res. **8**, 1 (1991).
36. K. Hillewaert, *Direct Numerical Simulation of the Taylor-Green Vortex at Re = 1600*, in *2nd International Workshop on High-Order CFD Methods* (Sponsored by DLR, AIAA and AFOSR, 2013).
37. U. Frisch, *Turbulence: The Legacy of A.N. Kolmogorov* (Cambridge University Press, 1995).
38. S. Jammy, C. Jacobs, N. Sandham, *Enstrophy and kinetic energy data from 3D Taylor-Green vortex simulations* `https://eprints.soton.ac.uk/401892/` (2016).
39. M. Lesieur, S. Ossia, J. Turbul. **1**, N7 (2000).
40. L. Skrbek, S. Stalp, Phys. Fluids **12**, 1997 (2000).
41. R. Stepanov, F. Plunian, M. Kessar, G. Balarac, Phys. Rev. E **90**, 053309 (2014).
42. P. Davidson, *Turbulence: An Introduction for Scientists and Engineers* (OUP Oxford, 2004).
43. P.L. O'Neill, D. Nicolaides, D. Honnery, J. Soria, *Autocorrelation Functions and the Determination of Integral Length with Reference to Experimental and Numerical Data*, in *Proceedings of 15th Australasian Fluid Mechanics Conference, 13–17 December 2004, The University of Sydney*, edited by M. Behnia, W. Lin, G. D. McBain (The University of Sydney, Sydney NSW, Australia, 2006) ISBN: 1-864-87695-6 (CD-ROM).